Not reviewed, for internal circulation only

# ATLAS NOTE

ATLAS-CONF-2012-032

March 12, 2012

# Measurement of the $t\bar{t}$ production cross section in the final state with a hadronically decaying tau lepton and jets using the ATLAS detector

The ATLAS Collaboration

**Abstract**

This document presents a measurement of the top quark pair ($t\bar{t}$) production cross section in the final state with a hadronically decaying tau lepton and jets. The analysis is based on proton-proton collision data corresponding to an integrated luminosity of 1.67 fb$^{-1}$ recorded by the ATLAS experiment at the LHC, with a center-of-mass energy of 7 TeV. The signal is extracted using a fit to the distribution of the number of tracks associated to the tau lepton candidate. The backgrounds from multijet events are modeled with data-driven methods. The $t\bar{t}$ production cross section is measured to be $\sigma_{t\bar{t}}$ = 200 ± 19 (stat.) ± 43 (syst.) pb.

# 1 Introduction

At the LHC, top quark pairs ($t\bar{t}$) are produced in abundance due to the high center-of-mass energy of $\sqrt{s}$ = 7 TeV. The large sample of $t\bar{t}$ events makes it possible to study experimentally challenging decay channels and topologies. This note describes a measurement of the $t\bar{t}$ production cross section; the studied topology consists of the final state with a hadronically decaying tau lepton and jets ($t\bar{t} \rightarrow \tau_{\mathrm{had}}$+jets). In this channel, one of the top quarks decays to a tau lepton, a $b$-quark and a neutrino, and the other top quark decays hadronically, as illustrated in Fig. 1. Such an event topology with a hadronically decaying tau lepton corresponds to 10% of all $t\bar{t}$ decays. This study provides a new measurement of the top quark pair cross section, which is also relevant for searches for processes beyond the Standard Model, in particular for charged Higgs production via top quark decays [1, 2, 3, 4]. The most recent cross section measurement of this decay channel has been made at $\sqrt{s}$ = 1.96 TeV at the Tevatron [5]. To this date, no other measurement in this specific channel has been conducted at $\sqrt{s}$ = 7 TeV.

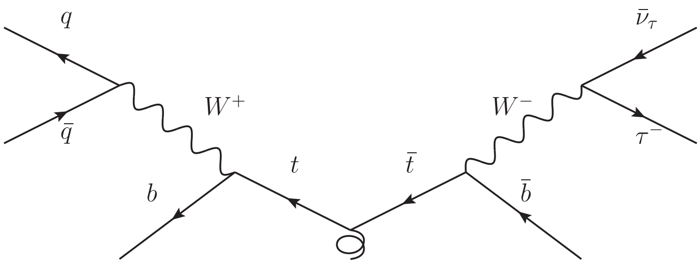


Figure 1: The $t\bar{t} \rightarrow \tau$ + jets topology. It consists of two $b$-quarks, two light quarks, and a tau lepton with its associated neutrino. The hadronic decay of the tau lepton produces one or three charged hadrons and a second tau neutrino. The escaping neutrinos from the $W$ and the subsequent tau lepton decay give rise to missing transverse energy.

In this analysis, events with at least five jets are selected, where two of the jets are identified as $b$-quark jets. One of the remaining jets is selected as the $\tau_{\mathrm{had}}$ candidate based on the event topology. The $\tau_{\mathrm{had}}$ contribution is separated from quark or gluon jets with a one-dimensional fit to the number of tracks associated with the $\tau_{\mathrm{had}}$ candidate. Since the $\tau_{\mathrm{had}}$ decays preferentially to 1 or 3 charged particles (and other neutral decay products), this variable offers a good separation between tau leptons and jets. The main backgrounds to the $t\bar{t}$ signal come from multijet events, from $t\bar{t}$ events with a different final state or from signal events where the wrong jet is chosen as the $\tau_{\mathrm{had}}$ candidate. A small contribution from single top and $W$+jets events is also present. The template distributions for the multijet and $t\bar{t}$ backgrounds used in the fit are obtained with data-driven methods.

This document is organized as follows. Section 2 gives a brief description of the ATLAS detector. Section 3 summarizes the data and Monte Carlo samples used for this study. Sections 4 and 5 list the event selection and the associated physics objects. A description of the signal and the expected sources of backgrounds is given in Section 6. Sections 7 and 8 describe the fit observable and the techniques used to obtain the templates. In Section 9, the results obtained by the fit, and the measurement of the cross section, are presented. Section 10 details the systematic uncertainties associated with the fit procedure and the cross section extraction. Finally, a summary of the results is given in Section 11.

## 2 Detector

The ATLAS detector [6] is a multipurpose particle physics apparatus with a forward-backward symmetric cylindrical geometry and a near $4\pi$ coverage in solid angle[1]. The inner tracking detector covers the pseudorapidity range $|\eta| < 2.5$, and consists of a silicon pixel detector, a silicon microstrip detector (SCT), and, for $|\eta| < 2.0$, a transition radiation tracker. The inner detector is surrounded by a thin superconducting solenoid providing a 2 T magnetic field. A high-granularity liquid-argon (LAr) sampling electromagnetic calorimeter covers the region $|\eta| < 3.2$. An iron-scintillator tile hadronic calorimeter provides coverage in the range $|\eta| < 1.7$. The end-cap and forward regions, spanning $1.5 < |\eta| < 4.9$, are instrumented with LAr calorimeters for both electromagnetic and hadronic measurements. The muon spectrometer surrounds the calorimeters. It consists of three large air-core superconducting toroid systems and stations of precision tracking chambers providing accurate muon tracking for $|\eta| < 2.7$. The trigger system consists of three levels which together reduce the event rate to about 200 Hz. The Level-1 trigger, implemented in hardware, identifies interesting high transverse momentum ($p_{\mathrm{T}}$) regions in the calorimeter and muon subsystems. This trigger is followed by two software-based trigger levels running more complex algorithms [7].

## 3 Data and Simulation Samples

The data used in this analysis were collected during the first half of the 2011 data taking period. They were recorded with stable beam conditions with all relevant subsystems fully operational, and correspond to a total integrated luminosity of $\mathcal{L} = 1.67\ \mathrm{fb}^{-1}$. The data sample has been selected with a $b$-jet trigger, which requires at least four jets with $|\eta| < 3.2$ and a transverse energy, $E_{\mathrm{T}}$, above 10 GeV identified by the Level-1 trigger, two of these jets being identified as $b$-jets using a dedicated high-level trigger $b$-tagging algorithm [7].

The analysis selection efficiency for the $t\bar{t} \to \tau_{had}$ + jets signal is derived from Monte Carlo (MC) simulations. For the generation of the $t\bar{t}$ signal, the `MC@NLO` v3.41 [8] generator with the parton distribution function (PDF) set `CT10` [9] is used. The $t\bar{t}$ cross section for proton-proton collisions at a centre-of-mass energy of $\sqrt{s} = 7$ TeV is $\sigma_{t\bar{t}} = 167^{+17}_{-18}$ pb for a top quark mass of 172.5 GeV. It has been calculated at approximate next-to-next-to-leading order (NNLO) in QCD with `Hathor 1.2` [10] using the `MSTW2008` 90% NNLO PDF sets [11], incorporating PDF+$\alpha_S$ uncertainties according to the `MSTW` prescription [12] and cross checked with the `NLO+NNLL` calculation of Cacciari et al. [13] as implemented in `Top++` 1.0 [14]. Tau lepton decays are modeled with `TAUOLA` [15]. MC samples are also used to correct for small contributions from $W$+jets, $Z$+jets, single top and diboson events, as described in Ref. [16]. The generated events were processed through the full ATLAS detector simulation based on `GEANT4` [17, 18], followed by the trigger and offline reconstruction. The distribution of the number of pile-up events (i.e. collisions in the same bunch crossing as the hard-scattering event) was adjusted to match the occupancies measured in the data.

## 4 Object Definition

Jets are reconstructed in the region $|\eta| < 4.5$ using the anti-$k_t$ algorithm [19, 20] with a distance parameter $R = 0.4$. The inputs to the jet reconstruction are topological clusters of calorimeter cells calibrated at

[1] ATLAS uses a right-handed coordinate system with its origin at the nominal interaction point (IP) in the center of the detector and the $z$-axis along the beam pipe. The $x$-axis points from the IP to the center of the LHC ring, and the $y$ axis points upward. Cylindrical coordinates $(r, \phi)$ are used in the transverse plane, $\phi$ being the azimuthal angle around the beam pipe. The pseudorapidity is defined in terms of the polar angle $\theta$ as $\eta = -\ln\tan(\theta/2)$. The variable $\Delta R$ is used to evaluate the distance between objects, and is defined as: $\Delta R = \sqrt{(\Delta\phi)^2 + (\Delta\eta)^2}$.

the electromagnetic (EM) energy scale [21]. A jet energy calibration based on $p_{\mathrm{T}}$ and $\eta$-dependent corrections derived from MC simulations and validated with data is applied. A detailed description of the jet reconstruction and calibration can be found in Ref. [22].

The identification of jets originating from $b$-quarks is performed using two likelihood-based algorithms, SV1 and IP3D [23]. The SV1 algorithm separates $b$-jets from light quark jets using secondary vertex properties, while the IP3D $b$-tagger uses the transverse and longitudinal impact parameters of each track within a jet. The SV1 and IP3D results are combined by multiplying their output likelihoods. The applied selection identifies $b$-jets with an average efficiency of 60% and provides a light quark jet rejection factor of about 340 in $t\bar{t}$ topologies. The likelihood of misidentifying a $\tau_{\mathrm{had}}$ as a $b$-jet in a $t\bar{t}$ event is approximately 5% [23].

The $\tau_{\mathrm{had}}$ candidate is selected from one of the jets reconstructed in the event and satisfying $p_{\mathrm{T}} >$ 40 GeV and $|\eta| < 2.5$. The $|\eta|$ range is determined by the acceptance of the tracking detectors while the $p_{\mathrm{T}}$ requirement is optimized to increase the background rejection. For each event, one $\tau_{\mathrm{had}}$ candidate is chosen following the procedure described in Section 5.

The missing transverse momentum $E_{\mathrm{T}}^{\mathrm{miss}}$ is calculated using all reconstructed physics objects (electrons, muons and jets) in the event, calibrated at their respective energy scale. Calorimeter clusters not associated to any object are also included, calibrated at the EM scale. The $E_{\mathrm{T}}^{\mathrm{miss}}$ significance $S_{E_{\mathrm{T}}^{\mathrm{miss}}}$ is defined as $E_{\mathrm{T}}^{\mathrm{miss}}/(0.5 \cdot \sqrt{\Sigma E_{\mathrm{T}}})$, where $\Sigma E_{\mathrm{T}}$ is the scalar sum of the transverse energy of all objects entering the $E_{\mathrm{T}}^{\mathrm{miss}}$ calculation.

The $t\bar{t} \to \tau_{\mathrm{had}}$+jets channel nominally has five jets and does not contain electrons or muons in the final state. Therefore, to reduce the backgrounds due to events containing $W$ bosons that decay leptonically and to avoid overlap with other $t\bar{t}$ cross section measurements, a veto against high-$p_{\mathrm{T}}$ leptons is applied as described in Section 5. The electrons used for this veto are required to pass a standard medium electron selection as defined in Ref. [24] with $p_{\mathrm{T}} > 15$ GeV and $|\eta| < 2.5$. Muons are reconstructed by combining tracks detected in the muon spectrometer and in the inner detector. Muon candidates with $p_{\mathrm{T}}$ $> 15$ GeV and $|\eta| < 2.5$ passing a standard medium muon selection are vetoed [25].

# 5 Event Selection

Candidate events are selected by applying the following requirements:

- at least 5 reconstructed jets with $p_{\mathrm{T}} > 20$ GeV and $|\eta| < 2.5$,
- no reconstructed electrons or muons,
- at least 2 jets in the event identified as $b$-jets,
- $S_{E_{\mathrm{T}}^{\mathrm{miss}}} > 8$.

The jet chosen as the $\tau_{\mathrm{had}}$ candidate for each event is selected according to the following procedure. Only jets with $p_{\mathrm{T}} > 20$ GeV and $|\eta| < 2.5$ are considered. First, the reconstruction of the hadronically decaying top is attempted by selecting the three jets (including exactly one $b$-jet among the two $b$-jets with the highest $b$-tag probability) which give the highest 4-vector $p_{\mathrm{T}}$ sum; these three jets are not considered as possible $\tau_{\mathrm{had}}$ candidates. The selection efficiency of this method is calculated in MC simulation by measuring the fraction of events in which the true $\tau_{\mathrm{had}}$ is not included in those three jets; this fraction is found to be $\sim 70\%$. The remaining jet with the highest $p_{\mathrm{T}}$, excluding the remaining $b$-jet among the two $b$-jets with the highest $b$-tag probability, is selected as the $\tau_{\mathrm{had}}$ candidate. This selection yields a total efficiency for identifying a $\tau_{\mathrm{had}}$ candidate of $\sim 50\%$.

# 6 Signal and Backgrounds

A summary of the expected number of events after the signal selection is given in Table 1. The last two rows show only events where the chosen candidate overlaps with a true $\tau_{\text{had}}$ (prompt) or electron (either prompt or from a leptonic tau decay). The contributions from the $t\bar{t}$ sample are separated into the last two columns; the first one contains all $t\bar{t}$ events, and the second one only events where a true $\tau_{\text{had}}$ ($p_{\text{T}} >$ 15 GeV, $|\eta| < 2.5$) is found.

The dominant components after the selection are: the signal ($\tau_{\text{had}}$ from $t\bar{t}$ events), electrons from $t\bar{t}$ events, jets from $t\bar{t}$, single $t$ and $Wb\bar{b}$ events, and jets from multijet and $b\bar{b}$ events. The contribution from $Z/\gamma$ + jets and diboson processes are negligible.

| | Multijets | $b\bar{b}$ | $W$+jets | $Wb\bar{b}$ | Single $t$ | All $t\bar{t}$ | $t\bar{t}$ with $\tau_{\text{had}}$ |
|---|---|---|---|---|---|---|---|
| Selected events | 293 | 757 | 4 | 41 | 36 | 691 | 299 |
| True $\tau_{\text{had}}$ | 0 | 0 | 1 | 10 | 10 | 150 | 149 |
| True $e$ | 0 | 0 | 0 | 3 | 2 | 44 | 3 |

Table 1: Expected number of events for signal and backgrounds for an integrated luminosity of 1.67 fb$^{-1}$. The $t\bar{t}$ contribution is split into the last two columns; the first one shows all events and the second one only events where a true $\tau_{\text{had}}$ with $p_{\text{T}} > 15$ GeV, $|\eta| < 2.5$ is selected. The last two rows show the number of events with $\tau_{\text{had}}$ candidates that could be matched to a true $\tau_{\text{had}}$ or electron; all other candidates being misidentified jets.

# 7 Fit Observable

Tau leptons decay hadronically 65% of the time [26], with ~ 77% of these decays producing only one charged hadron and ~ 23% producing three charged hadrons. This gives rise to a typical detector signature: a calorimeter energy deposition matched to one or three charged particle tracks, whereas jets from multijet background processes typically have a larger track multiplicity. Therefore, the number of charged particle tracks associated to a jet is an excellent variable to separate $\tau_{\text{had}}$ candidates from the backgrounds.

To determine the number of tracks associated with a $\tau_{\text{had}}$ candidate, tracks are selected using the following quality criteria:

- $|d_0| < 1$ mm, where $d_0$ is the transverse impact parameter with respect to the primary vertex,
- $|z_0 \cdot \sin\theta| < 1.5$ mm, where $z_0$ is the longitudinal impact parameter with respect to the primary vertex,
- number of hits in the innermost pixel barrel layer $\geq 1$,
- number of pixel hits $\geq 2$,
- number of pixel hits + number of SCT hits $\geq 7$.

All selected tracks with $p_{\text{T}} > 1$ GeV located in a core region of size $\Delta R < 0.2$ around the jet axis are counted. To increase the discriminating power, a $k_t$-like algorithm is used to count tracks with $p_{\text{T}} >$ 500 MeV in the outer cone $0.2 < \Delta R < 0.6$ [27]. The sum of these core and outer tracks is labeled $n_{track}$, and is used as the fit variable. The separation potential of this variable is illustrated in Fig. 2 where a comparison of the $n_{track}$ distribution is shown for $\tau_{\text{had}}$ and multijet events.

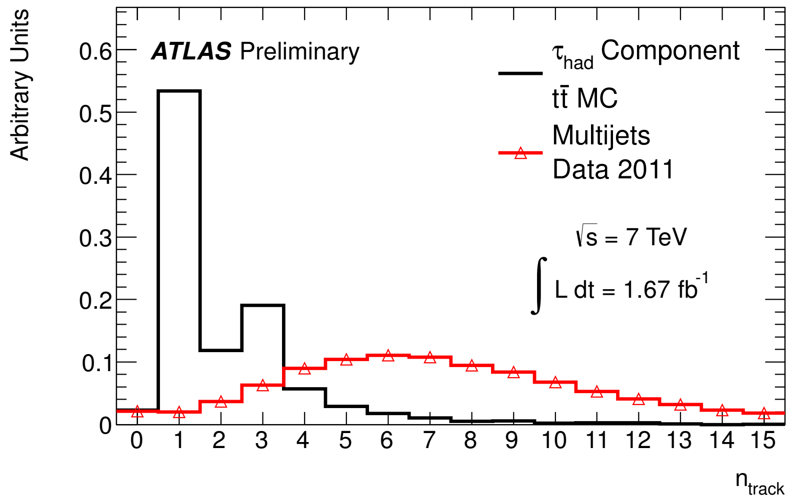


Figure 2: Distribution of $n_{track}$ for true $\tau_{\mathrm{had}}$ from MC $t\bar{t}$ events (black line) and for jets from multijet events from data (red triangles).

# 8 Signal and Background Templates

To extract the signal from the $n_{track}$ distribution, the data sample is fitted with three templates, i.e. a *tau & electron* template, a *multijets* template and a *combinatorics* template.

The $\tau_{\mathrm{had}}$ component from $t\bar{t}$ events is the actual signal contribution. Real electrons (either prompt or from leptonic tau decays) from $t\bar{t}$ events also contribute significantly to the signal region. Because the main differences in the electron and $\tau_{\mathrm{had}}$ templates are in bins where backgrounds are expected to dominate, they are combined into a single *tau & electron* template to ensure a stable fit. After the fit is performed, the expected contribution to the *tau & electron* template from non-$t\bar{t}$ events is subtracted. The electron component is also subtracted to obtain the number of $\tau_{\mathrm{had}}$ from the signal. The *tau & electron* template is taken from simulated $t\bar{t}$ events; the two separate components of this template are shown in Fig. 3. The small expected contributions to the real $\tau_{\mathrm{had}}$ component of the fit from single top and $Wb\bar{b}$ do not change the shape of the template.

The remaining significant contributions come from jets, both from $t\bar{t}$ events (*combinatorics*) and multijet events (*multijets*). The *multijets* sample is dominated by gluon-initiated jets which have a higher track multiplicity than the quark-initiated jets dominating the *combinatorics* sample. To describe both contributions, a data-driven method is used.

The *combinatorics* template is taken from a $t\bar{t}$ control sample where the $\tau_{\mathrm{had}}$ candidate is replaced by a muon candidate (this is referred to as the $t\bar{t}\,\mu$+jets control sample). The muon is required to pass a tight muon selection [25], $p_{\mathrm{T}} > 20$ GeV, $|\eta| < 2.5$ and have no jet with $p_{\mathrm{T}} > 20$ GeV within $\Delta R < 0.4$. The requirement on the number of non $b$-tagged jets is changed from three to two as the jet corresponding to the $\tau_{\mathrm{had}}$ is now replaced by a muon. The other selection requirements are the same as described in Section 5. This isolates $t\bar{t}$ events with very high purity: the contribution from backgrounds is at the $\sim 5\%$ level, mainly from single top and $W$+jets events. To increase the statistics, the two highest $p_{\mathrm{T}}$ non $b$-tagged jets are selected as $\tau_{\mathrm{had}}$ candidates. As the $n_{track}$ distribution is $p_{\mathrm{T}}$ dependent, the template is corrected for the difference in kinematics introduced by the inclusion of the second-leading jet. It is further corrected to remove the expected contribution (from MC simulation) from $t\bar{t}$ dilepton events ($t\bar{t} \to \mu + \tau_{\mathrm{had}} + X$, $t\bar{t} \to \mu + e + X$) with real $\tau_{\mathrm{had}}$ and electrons in the final state. This procedure is tested with simulated events and observed deviations between the $t\bar{t}\,\mu$ + jets and $t\bar{t}\,\tau_{\mathrm{had}}$ + jets samples

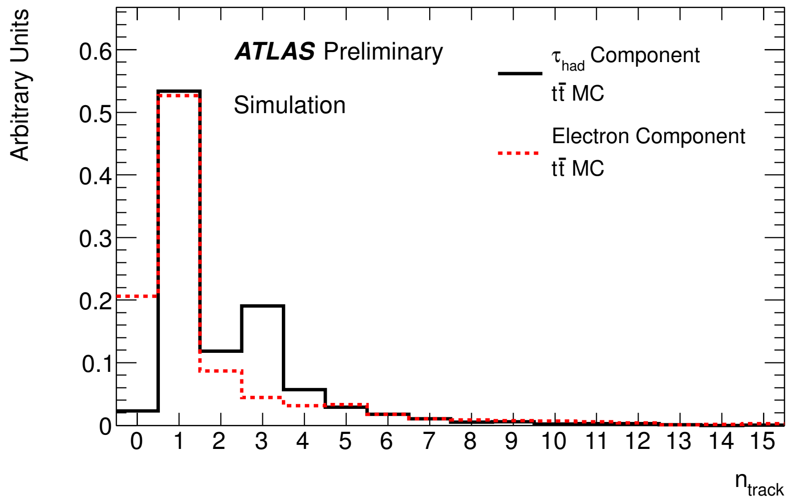


Figure 3: Distribution of $n_{track}$ for $\tau_{\text{had}}$ (solid black line) and electrons (dashed red line) from MC $t\bar{t}$ samples.

are taken as a systematic uncertainty; the results of this test are shown in Fig. 4. The small contributions of misidentified jets from single top and $Wb\bar{b}$ are taken into account; the resulting change in the template shape is negligible.

The *multijets* template is modeled using a sideband region where the $S_{E_{\mathrm{T}}^{\mathrm{miss}}}$ requirement is lowered to $3 < S_{E_{\mathrm{T}}^{\mathrm{miss}}} < 4$. This selection greatly enhances the contribution from multijet events, reducing other contributions (e.g. from $t\bar{t}$ events) to less than 1%. The assumption that the $n_{track}$ distribution for *multijets* events is independent of the $S_{E_{\mathrm{T}}^{\mathrm{miss}}}$ has been verified both with MC simulation over the entire $S_{E_{\mathrm{T}}^{\mathrm{miss}}}$ range, and with data, using the $2 < S_{E_{\mathrm{T}}^{\mathrm{miss}}} < 3$ and $4 < S_{E_{\mathrm{T}}^{\mathrm{miss}}} < 5$ sideband regions which are also multijet

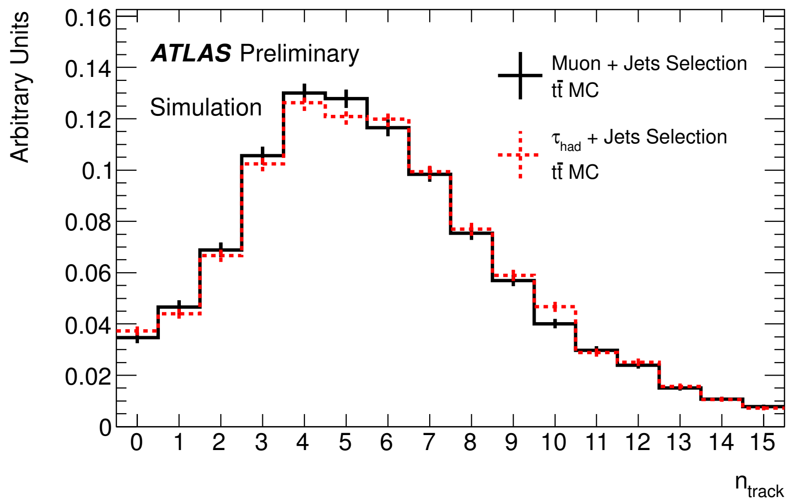


Figure 4: The $n_{track}$ distribution for the *combinatorics* background. The solid black line refers to the template obtained using a simulated $t\bar{t}$ $\mu$+jets control sample, and the dashed red line refers to the *combinatorics* jets expected from the signal events, also taken from MC simulation. The error bars represent the statistical uncertainties due to the MC sample size.

enriched. Figure 5 shows a comparison of the *multijets* templates obtained from these three separate control samples.

Possible sources of mismodeling in the template shapes and the corresponding systematic uncertainties are discussed in Section 10.



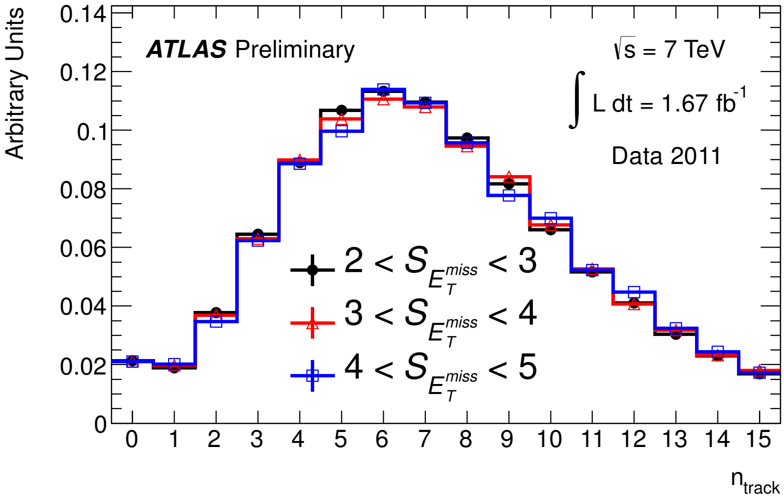


Figure 5: The *multijets* templates obtained from three different $S_{E_T^{miss}}$ regions in the data. The black circles, red triangles and blue squares refer to the $2 < S_{E_T^{miss}} < 3$, $3 < S_{E_T^{miss}} < 4$ and $4 < S_{E_T^{miss}} < 5$ control regions, respectively.

# 9 Results

An extended binned-likelihood fit is used to extract the number of *tau & electron* events from the $n_{track}$ distribution. To improve the fit stability, the number of *combinatorics* events is constrained to the number of *tau & electron* events, using a Gaussian term. Both contributions come from the same process ($t\bar{t}$ events), and their relative production rate is consequently well understood. The fit is implemented using the `ROOFit` package [28]. The statistical uncertainties on the fit parameters are calculated using the shape of the fit likelihood. The systematic uncertainties on the shapes of the templates are propagated using a pseudo-experiment approach, taking into account the bin-by-bin correlations. The fit to the data sample is repeated for every set of templates corresponding to the systematics variations discussed in Section 10. The mean number of *tau & electron* events over the pseudo-experiment ensemble is taken as the main result, and the RMS of this distribution is taken as the total systematic uncertainty on the fit. This yields a final result of 268 ± 24 (stat.) ± 17 (syst.). The fits returns an average $\chi^2$ per degree of freedom of 1.5 (using statistical uncertainties only) over the ensemble of pseudo-experiments.

Figure 6 shows the fit results. Table 2 presents a comparison between the fit results, and the expected event yields from the MC predictions. The numbers are in good agreement.

To extract the number of signal events, a total of 12 ± 3 (from single top) and 13 ± 14 (from $Wb\bar{b}$) background events, as predicted by the simulation, are subtracted from the fitted number of *tau & electron* predictions. The contributions from all other Standard Model backgrounds are negligible. The obtained number is then scaled by the expected ratio of $\tau_{\rm had}$ and electrons passing the selection in the $t\bar{t}$ sample. This ratio, $\frac{N_\tau}{N_\tau+N_e}$, is estimated from MC simulation to be 0.77 ± 0.03 (stat.) ± 0.03 (syst.). This yields a final number of observed signal events of: $N_\tau$ = 188 ± 22 (stat.) ± 15 (syst.).

Not reviewed, for internal circulation only

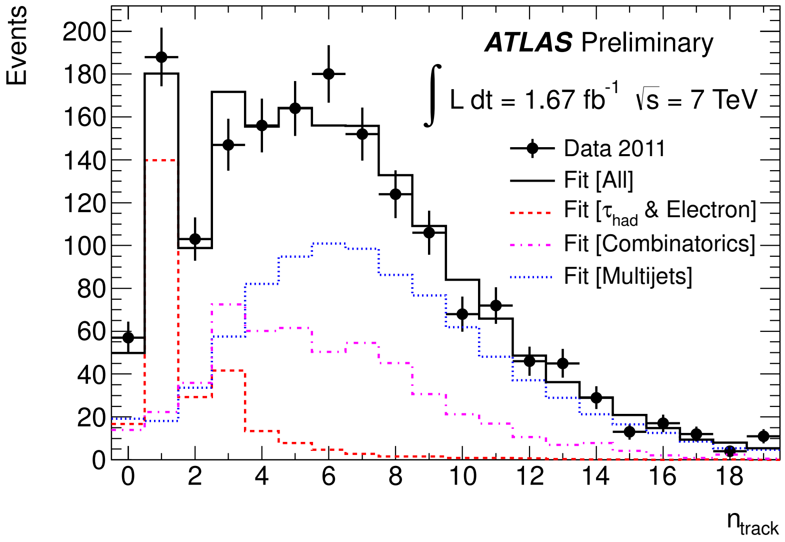


Figure 6: The $n_{track}$ distribution for $\tau_{\text{had}}$ candidates after all selection cuts. The black circles correspond to data, while the solid histogram is the result of the fit. The red, blue and magenta dashed curves show the fitted contributions from *tau & electron* "signal", and the *multijets* and *combinatorics* backgrounds, respectively.

| Source | Number of events |
|---|---|
| $t\bar{t}$ ($\tau_{\text{had}}$) | 150 ± 30 |
| $t\bar{t}$ (electrons) | 44 ± 9 |
| Single top | 12 ± 3 |
| $Wb\bar{b}$ | 13 ± 14 |
| Total expected | 219 ± 34 |
| Fit results | 268 ± 24 (stat.) ± 17 (syst.) |

Table 2: Comparison of the numbers of *tau & electron* events from MC expectations and from the results of the fit to the data.

The cross section is obtained from:

$$\sigma_{t\bar{t}} = \frac{N_\tau}{\mathcal{L} \cdot \varepsilon}. \tag{1}$$

The efficiency ($\varepsilon$) is estimated from MC simulation to be (5.6 ± 1.1) $\times 10^{-4}$. It includes the branching fractions for the different $t\bar{t}$ decays and the associated acceptances. The efficiency is corrected for the flavor dependence of the $W$ branching ratios [26], as this effect is not taken into account in the simulated event samples. It is also corrected for a 10% total difference between MC simulation and data in the trigger and $b$-tagging efficiencies [23]. The method used for obtaining the uncertainty on this number is detailed in Section 10.2. Using Eq. (1), the following cross section is obtained:

$$\sigma_{t\bar{t}} = 200 \pm 19\,(\text{stat.}) \pm 43\,(\text{syst.})\,\text{pb}. \tag{2}$$

# 10 Systematic Uncertainties

The systematic uncertainties on the cross section measurement presented in this document are separated into two categories. The fit uncertainties affect the fitted number of signal events as described above. The efficiency uncertainties come into play when the cross section is calculated from the number of signal events and Eq. (1).

## 10.1 Fit Uncertainties

Several possible sources of mismodeling are taken into account when estimating the uncertainty on the shape of the templates. Each uncertainty is modeled separately and bin-to-bin correlations are taken into account. The effect of each systematic uncertainty on the fitted number of $\tau_{\text{had}}$ and electron events for each template is summarized in Table 3.

| Source of uncertainty | $\Delta n_{tau\&electron}$ (relative) |
|---|---|
| *tau & electron* template | |
| $\tau_{\text{had}}$/e ratio | < 1% |
| Statistical uncertainty | 1% |
| Jet energy scale | < 1% |
| Pile-up | 1% |
| ISR/FSR | 5% |
| Track reconstruction | < 1% |
| *combinatorics* template | |
| Closure in simulation | 2% |
| Dilepton subtraction | 1% |
| Statistical uncertainties (data) | 4% |
| Statistical uncertainties (Monte Carlo) | 1% |
| $p_{\text{T}}$ reweighting | < 1% |
| *multijets* template | |
| Closure to $2 < S_{E_{\text{T}}^{\text{miss}}} < 3$ sideband | 1% |
| Closure to $4 < S_{E_{\text{T}}^{\text{miss}}} < 5$ sideband | < 1% |
| Statistical uncertainties ($2 < S_{E_{\text{T}}^{\text{miss}}} < 3$) | < 1% |
| Statistical uncertainties ($3 < S_{E_{\text{T}}^{\text{miss}}} < 4$) | < 1% |
| Statistical uncertainties ($4 < S_{E_{\text{T}}^{\text{miss}}} < 5$) | 1% |
| Total fit uncertainty | 7% |

Table 3: Systematic uncertainties on the fitted number of signal events. The relative uncertainties on the fit parameter ($\Delta n_{tau\&electron}$) are quoted.

The *tau & electron* template is taken from MC-simulated $t\bar{t}$ events. As the $\tau_{\text{had}}$ decay is an electroweak process, and the $\tau_{\text{had}}$ leaves the interaction region before decaying, hadronization and fragmentation models do not play a significant role in the simulation of the $n_{track}$ distribution. Most of the sources of mismodeling therefore come from detector effects and the underlying event environment. The effects due to the uncertainty on the track reconstruction performance are taken into account by studying an alternative MC sample with modified dead material in the inner detector. MC samples with variations in the amount of initial and final state radiation (ISR/FSR) are used to estimate the probability of additional tracks being reconstructed close to the $\tau_{\text{had}}$ candidate; the parameters governing the ISR/FSR for these samples are varied in a range consistent with experimental data [29]. The effects of the jet energy scale uncertainty on the $p_{\mathrm{T}} > 40$ GeV requirement are also taken into account [22]. The change in template shape due to the imperfect simulation of the electron reconstruction leads to a different ratio of $\tau_{\mathrm{had}}$ to electrons in simulation and data. It is estimated by using the uncertainties on the efficiency of the electron veto. An uncertainty on the effect of pile-up tracks on the template shape is obtained by reweighting the MC samples using different methods (reweighted to the number of reconstructed primary vertices instead of the average number of interactions). This procedure is known to provide conservative estimates of the pile-up effects. The uncertainty due to the limited size of the simulated event samples is also taken into account.

The *combinatorics* template is obtained from the $t\bar{t}$ $\mu$+jets control sample in data. The uncertainty due to the small differences in shapes between the template obtained from the data-driven method and the expected distribution is estimated from the $t\bar{t}$ MC sample, as shown in Fig. 4. This is referred to as the closure uncertainty. The dilepton contribution (real $\tau_{\mathrm{had}}$ and electrons in the template coming from dilepton $t\bar{t}$ events) is subtracted using MC estimates. A relative uncertainty of 26% is taken on this fraction, obtained using the same method as used for the efficiency (see Section 10.2). The statistical uncertainties of the data sample and of the MC sample used to estimate the closure are both included. Finally, the effect of the jet energy scale uncertainty on the $p_{\mathrm{T}}$ correction is also taken into account.

The *multijets* template is derived from a background-dominated sideband region with low $S_{E_{\mathrm{T}}^{\mathrm{miss}}}$. The $n_{track}$ distributions depend on the jet flavor and jet kinematics. However, different $S_{E_{\mathrm{T}}^{\mathrm{miss}}}$ criteria do not affect the $n_{track}$ distributions (see Fig. 5). For this reason, an estimate of the closure uncertainty of this method is taken from the comparison between three different $S_{E_{\mathrm{T}}^{\mathrm{miss}}}$ regions ($2 < S_{E_{\mathrm{T}}^{\mathrm{miss}}} < 3$, $3 < S_{E_{\mathrm{T}}^{\mathrm{miss}}} < 4$, and $4 < S_{E_{\mathrm{T}}^{\mathrm{miss}}} < 5$), where multijet background events dominate, as all other sources have a contribution of less than 1%. The statistical uncertainties of the data sideband regions are also taken into account.

The total systematic uncertainty on the fit is found to be 7%.

## 10.2 Efficiency Uncertainty

A summary of the uncertainties affecting the MC signal efficiency calculation is given in Table 4.

| Source of uncertainty | Relative uncertainty |
|---|---|
| ISR/FSR | 12% |
| Choice of hadronization model | 7% |
| Choice of event generator | 2% |
| PDFs | 2% |
| $E_{\mathrm{T}}^{\mathrm{miss}}$ significance mismodeling | 5% |
| Jet energy scale | 6% |
| Jet reconstruction efficiency | < 1% |
| Jet energy resolution | 2% |
| $b$-jet tagging efficiency | 10% |
| $b$-jet trigger efficiency | 3% |
| Light jet mistag rate | < 1% |
| Electron veto | < 1% |
| Muon veto | < 1% |
| Pile-up | 1% |
| Luminosity | 4% |
| Total $\varepsilon$ uncertainty | 19% |

Table 4: Systematic uncertainties on the estimated signal efficiency.

The uncertainty due to the choice of event generation configuration is estimated by using alternative

Not reviewed, for internal circulation only

MC samples and reweighting procedures. The difference in the efficiency obtained from different configurations is taken as the uncertainty. The full details of the samples, generators and procedures used for this study are documented in greater detail in Ref. [16]. The effect of the possible mismodeling of the ISR/FSR is taken into account by using `AcerMC` samples with specific tunes aimed at conservatively varying the amount of parton showering. To study the impact of different hadronization models, events generated using `POWHEG` are processed with two different hadronization programs: `Herwig` interfaced to `Jimmy` and `Pythia`. The uncertainty due to the choice of the matrix element event generator is estimated by comparing $t\bar{t}$ samples generated using `MC@NLO` and `POWHEG`. To estimate the effect of the PDFs on the efficiency, the nominal $t\bar{t}$ MC sample is reweighted using three different PDF sets (`CT10`, `MSTW2008` and `NNPDF20` [30]) with their associated error eigenvectors.

The uncertainties on the simulation of the detector response are listed below. The energy of jets is varied based on the jet energy scale uncertainty [22]. The effect of the uncertainty on the jet reconstruction efficiency is estimated based on results from data studies. The impact of a non-perfect modeling of the jet energy resolution is evaluated by including additional smearing in the energies of simulated jets. The efficiency and rejection of the $b$-tagging algorithm has been estimated in data and and corrections as a function of jet flavor, $p_{\mathrm{T}}$ and $\eta$ [23] have been included in the simulation. The trigger efficiency is measured with data using the $t\bar{t}\,\mu$+jets control sample. The uncertainty due to a possible mismodeling of the muon and electron vetoes is estimated using the uncertainties on their respective reconstruction efficiencies. As both variables used in the calculation of $S_{E_{\mathrm{T}}^{\mathrm{miss}}}$, $E_{\mathrm{T}}^{\mathrm{miss}}$ and $\Sigma\,E_{\mathrm{T}}$, depend on all reconstructed objects in the event, these quantities must be recalculated to account for the systematic uncertainties on the energy measurements of these objects. The uncertainties on the energy of jets and energy clusters outside reconstructed jets are propagated to the $E_{\mathrm{T}}^{\mathrm{miss}}$ calculation. This estimate is further validated with the $t\bar{t}\,\mu$+jets control sample, and the deviations are found to be within the quoted uncertainties.

The uncertainty due to the modeling of the pile-up is determined as described in Section 10.1. The luminosity uncertainty is 4% [31].

## 11 Summary and Conclusions

This document presents a measurement of the top quark pair production cross section in the final state with one hadronically decaying tau lepton and jets. The measurement uses a dataset corresponding to an integrated luminosity of 1.67 fb$^{-1}$of proton-proton collision data recorded by the ATLAS experiment. A method based on fitting the distribution of the number of tracks associated to the tau lepton candidate with templates is used, where the background shapes are derived from data.

The $t\bar{t}$ production cross section is measured to be: $\sigma_{t\bar{t}}$ = 200 ± 19 (stat.) ± 43 pb. This result is in agreement with the theoretical prediction of $167^{+17}_{-18}$ pb, as well as the latest combination of different ATLAS analyses yielding 177 ± 3 (stat.) $^{+8}_{-7}$ (syst.) ± 7 (lumi.) pb [32].

## 12 References


[1] J. F. Gunion, H. E. Haber, G. Kane, and S. Dawson, *The Higgs Hunter's Guide*. Addison-Wesley, 1990.

[2] J. F. Gunion, H. E. Haber, G. Kane, and S. Dawson, *Errata for "The Higgs Hunter's Guide"*, preprint SCIPP-92-58, 1993. `arXiv:hep-ph/9302272 [hep-ph]`.

[3] J. F. Gunion and H. E. Haber, *Higgs Bosons in Supersymmetric Models*, Nucl. Phys. **B272** (1986) 1.

[4] ATLAS Collaboration, *Search for charged Higgs bosons decaying via $H^{\pm} \to \tau\nu$ in $t\bar{t}$ events using 4.6 $fb^{-1}$ of pp collision data at $\sqrt{s}$ = 7 TeV with the ATLAS detector*, ATLAS-CONF-2012-011, https://cdsweb.cern.ch/record/1429659, 2012.

[5] V. M. Abazov et al., *Measurement of $t\bar{t}$ production in the $\tau$ + jets topology using $p\overline{p}$ collisions at $\sqrt{s}$ = 1.96 TeV*, Phys. Rev. **D82** (2010) 071102, arXiv:1008.4284 [hep-ex].

[6] ATLAS Collaboration, *The ATLAS Experiment at the CERN Large Hadron Collider*, JINST **3** (2008) S08003.

[7] ATLAS Collaboration, *Performance of the ATLAS Trigger System in 2010*, Eur. Phys. J. **C72** (2012) 1849.

[8] S. Frixione and B. R. Webber, *Matching NLO QCD computations and parton shower simulations*, JHEP **06** (2002) 029, arXiv:hep-ph/0204244 [hep-ph].

[9] H.-L. Lai et al., *New parton distributions for collider physics*, Phys. Rev. **D82** (2010) 074024, arXiv:1007.2241 [hep-ph].

[10] M. Aliev, H. Lacker, U. Langenfeld, S. Moch, and P. Uwer, *HATHOR: HAdronic Top and Heavy quarks crOss section calculatoR*, Comput. Phys. Commun. **182** (2011) 1034–1046, arXiv:1007.1327 [hep-ph].

[11] A. D. Martin, W. J. Stirling, R. S. Thorne, and G. Watt, *Parton distributions for the LHC*, Eur. Phys. J. **C63** (2009) 189–285, arXiv:0901.0002 [hep-ph].

[12] A. Martin, W. Stirling, R. Thorne, and G. Watt, *Uncertainties on alpha(S) in global PDF analyses and implications for predicted hadronic cross sections*, Eur. Phys. J. **C64** (2009) 653–680, arXiv:0905.3531 [hep-ph].

[13] M. Cacciari, M. Czakon, M. L. Mangano, A. Mitov, and P. Nason, *Top-pair production at hadron colliders with next-to-next-to-leading logarithmic soft-gluon resummation*, CERN-PH-TH-2011-277, TTK-11-54, 2011. arXiv:1111.5869 [hep-ph].

[14] M. Czakon and A. Mitov, *Top++: a program for the calculation of the top-pair cross-section at hadron colliders*, 2011. arXiv:1112.5675 [hep-ph].

[15] S. Jadach, Z. Was, R. Decker, and J. H. Kuhn, *The $\tau$ decay library TAUOLA, version 2.4*, Comput. Phys. Commun. **76** (1993) 361–380.

[16] ATLAS Collaboration, *Measurement of the top quark-pair production cross section with ATLAS in pp collisions at $\sqrt{s}$ = 7 TeV*, Eur. Phys. J. **C71** (2011) 1577, arXiv:1012.1792 [hep-ex].

[17] GEANT4 Collaboration, S. Agostinelli et al., *GEANT4: A simulation toolkit*, Nucl. Instrum. Meth. **A506** (2003) 250–303.

[18] ATLAS Collaboration, *The ATLAS Simulation Infrastructure*, Eur. Phys. J. **C70** (2010) 823–874, arXiv:1005.4568 [physics.ins-det].

[19] M. Cacciari and G. P. Salam, *Dispelling the $N^3$ myth for the $k_t$ jet-finder*, Phys. Lett. **B641** (2006) 57–61, arXiv:hep-ph/0512210 [hep-ph].

[20] M. Cacciari, G. P. Salam, and G. Soyez, *The anti-$k_t$ jet clustering algorithm*, JHEP **0804** (2008) 063, arXiv:0802.1189 [hep-ph].

[21] ATLAS Collaboration, *Calorimeter Clustering Algorithms: Description and Performance*, ATL-LARG-PUB-2008-002, `https://cdsweb.cern.ch/record/1099735`, 2008.

[22] ATLAS Collaboration, *Jet energy measurement with the ATLAS detector in proton-proton collisions at $\sqrt{s} = 7$ TeV*, CERN-PH-EP-2011-191, 2011. `arXiv:1112.6426 [hep-ex]`. Submitted to Eur. Phys. J. C.

[23] ATLAS Collaboration, *Commissioning of the ATLAS high-performance b-tagging algorithms in the 7 TeV collision data*, ATLAS-CONF-2011-102, `https://cdsweb.cern.ch/record/1369219`, 2011.

[24] ATLAS Collaboration, *Electron performance measurements with the ATLAS detector using the 2010 LHC proton-proton collision data*, CERN-PH-EP-2011-117, 2011. `arXiv:1110.3174 [hep-ex]`. Accepted by Eur. Phys. J. C.

[25] ATLAS Collaboration, *Muon reconstruction efficiency in reprocessed 2010 LHC proton-proton collision data recorded with the ATLAS detector*, ATLAS-CONF-2011-063, `https://cdsweb.cern.ch/record/1345743`, 2011.

[26] Particle Data Group Collaboration, K. Nakamura et al., *Review of particle physics*, J. Phys. **G37** (2010) 075021.

[27] ATLAS Collaboration, *Performance of the Reconstruction and Identification of Hadronic Tau Decays with ATLAS*, ATLAS-CONF-2011-152, `https://cdsweb.cern.ch/record/1398195`, 2011.

[28] W. Verkerke and D. Kirkby, *The RooFit toolkit for data modeling*, in *Proceedings of 2003 Conference for Computing in High-Energy and Nuclear Physics (CHEP 03)*, no. MOLT007. `http://www.slac.stanford.edu/econf/C0303241/`, 2003. `arXiv:physics/0306116`.

[29] ATLAS Collaboration, *Expected Performance of the ATLAS Experiment — Detector, Trigger and Physics*, pp 15-697, pp 869–882, 2009. `arXiv:0901.0512 [hep-ex]`.

[30] R. D. Ball, V. Bertone, F. Cerutti, L. Del Debbio, S. Forte, et al., *Impact of Heavy Quark Masses on Parton Distributions and LHC Phenomenology*, Nucl. Phys. **B849** (2011) 296–363, `arXiv:1101.1300 [hep-ph]`.

[31] ATLAS Collaboration, *Luminosity Determination in pp Collisions at $\sqrt{s} = 7$ TeV using the ATLAS Detector in 2011*, ATLAS-CONF-2011-116, `https://cdsweb.cern.ch/record/1376384`, 2011.

[32] ATLAS Collaboration, *Statistical combination of top quark pair production cross-section measurements using dilepton, single-lepton, and all-hadronic final states at $\sqrt{s} = 7$ TeV with the ATLAS detector*, ATLAS-CONF-2012-024, `http://cdsweb.cern.ch/record/1430733`, 2012.